




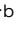




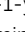
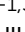
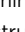
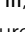
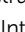



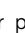

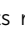
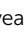
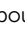
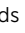
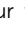

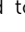
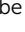
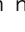
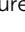




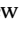
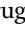

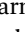
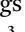
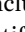
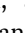
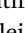
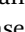
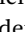
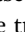
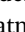


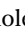

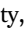
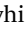
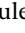
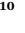
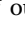
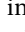
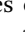
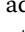
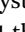
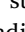
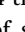
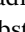

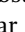


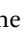

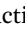
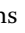
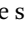
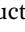
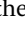
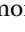
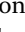
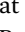
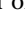
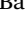





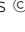





Cite this: *RSC Adv.*, 2020, 10, 9840

Quantitative assessment of the nature of noncovalent interactions in *N*-substituted-5-(adamantan-1-yl)-1,3,4-thiadiazole-2-amines: insights from crystallographic and QTAIM analysis†

Ali A. El-Emam,^a Elangovan Saveeth Kumar,^b Krishnakumar Janani,^b Lamyia H. Al-Wahaibi,^c Olivier Blacque,^d Mohamed I. El-Awady,^e Nora H. Al-Shaalan,^c M. Judith Percino^f and Subbiah Thamotharan^g                                                                                      

molecules (QTAIM) framework.¹⁴ The noncovalent bonding nature and character (HB and van der Waals interactions) were assessed by first four criteria of Koch–Popelier.¹⁵

These four criteria are (i) topology (BCP), (ii) electron density $\rho(r)$ at the BCP (iii) Laplacian of the electron density $\nabla^2\rho(r)$ and (iv) mutual penetration of the H and the acceptor atom. The fourth criterion of KP (hereafter KP-4) compares the bonding (r_D and r_A) and non-bonding radii of donor (r_D^0) and acceptor atoms (r_A^0). The bonding radii are taken as length from the BCP to the nuclei, whereas non-bonding radii of hydrogen and the acceptor atoms are taken as the gas phase van der Waals radii.¹⁶ The strong and weak intermolecular interactions in different molecules have been quantitatively analyzed using the first four criteria of KP successfully.¹⁷ The strength of various noncovalent interactions at their BCPs in these three structures was quantified using an empirical scheme [$D_e = -0.5 \times V(r)$] proposed by EML¹⁸ and the total electronic energy density $H(r)$ [$H(r) = V(r) + G(r)$; where $V(r)$ and $G(r)$ represent potential energy density and kinetic energy density] proposed by Cremer & Kraka.¹⁹ In the bromo derivative, we observed a homo-halogen (Br \cdots Br) contact and found to be important for stabilization. We report herein a detailed CSD (Cambridge Structural Database) analysis of Br \cdots Br interaction to know its geometrical preferences.

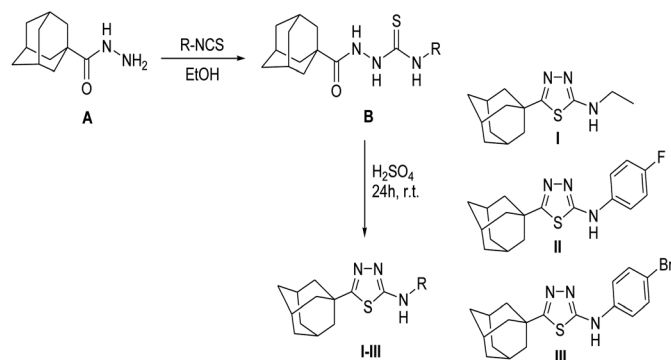
Experimental

Synthesis and crystallization

The title *N*-substituted-5-(adamantan-1-yl)-1,3,4-thiadiazole-2-amines **I**, **II** and **III** were synthesized starting with adamantane-1-carbohydrazide **A** *via* treatment with the appropriate isothiocyanate to yield the corresponding 1-[(1-adamantan-1-yl)carbonyl]-4-substituted thiosemicarbazides **B**, which were cyclized to their 1,3,4-thiadiazole analogues **I–III** using sulphuric acid at room temperature for 24 hours (Scheme 1).²⁰ Pure single crystals for X-ray analysis were obtained by slow evaporation of CHCl₃ : EtOH (1 : 1) solution at room temperature. A detailed synthesis procedure and ¹H NMR spectral data for compounds **I–III** are given in ESI.†

Single crystal X-ray structure determination

The selected suitable single crystals of compounds **I–III** were mounted using polybutene oil on a flexible loop fixed on



Scheme 1 The synthetic pathway for the target compounds **I–III**.

a goniometer head and immediately transferred to the diffractometer. Single crystal X-ray diffraction data were collected on a Rigaku OD XtaLAB Synergy, Dualflex Pilatus 200 K diffractometer using a single wavelength X-ray source (Cu K α radiation: $\lambda = 1.54184$ Å) (Rigaku Oxford Diffraction, 2015) from a micro-focus sealed X-ray tube and an Oxford liquid-nitrogen Cryostream cooler. Pre-experiment, data collection, data reduction and analytical absorption correction²¹ were performed with the program suite CrysAlisPro (CrysAlisPro (Version 1.171.40.16c), Rigaku Oxford Diffraction, 2018) using Olex2, a complete structure solution, refinement and analysis program.²² The structures were solved with the SHELXT small molecule structure solution program.²³ All non-hydrogen atoms were refined with the SHELXL 2018/3 program package by full-matrix least-squares minimization on F^2 .²⁴ The position of amine H atom was located from a difference Fourier map and freely refined. In compound **I**, the methyl H were constrained to an ideal geometry with C–H = 0.98 Å and $U_{iso}(H) = 1.5U_{eq}(C)$, but were allowed to rotate freely about the C–C bond. The remaining H atoms were placed in calculated geometrical positions with C–H = 0.93–1.00 Å and $U_{iso}(H) = 1.2U_{eq}(C)$.

Hirshfeld surface analysis

The Hirshfeld surface analysis has been performed with CrystalExplorer-17.5 program using the X-ray geometries after normalizing the H involving distances with N–H = 1.009 and C–H = 1.083 Å.²⁵ The interatomic contacts were visualized on the Hirshfeld surface using three different colour (red-white-blue) scales. The red-white-blue colour schemes were used to identify the interatomic contact distances are shorter than vdW separation (red), equal to vdW separation (white) and longer than vdW separation (blue) from the Hirshfeld surface that was mapped over the function of d_{norm} . 2D-fingerprint plots were obtained from the Hirshfeld surface analysis in order to compute the relative contributions of different intermolecular interactions exist in the crystal structures.

PIXEL energy calculation

Intermolecular interaction energies for different dimers in the crystal structures of **I–III** and lattice energies for these compounds were calculated using the PIXELC module of CLP program.¹³ The intermolecular interaction energy (E_{tot}) is the sum of the coulombic (E_{coul}), polarization (E_{pol}), dispersion (E_{disp}) and repulsion (E_{rep}) energy terms. The X-ray geometries were used after the normalizing the H involving bond lengths as mentioned above. For the PIXEL calculation, the electron density of the molecules of **I–III** has been calculated at MP2/6-31G** level of theory using Gaussian program.²⁶

DFT computation and QTAIM analysis

All the quantum chemical calculations were performed with the program Gaussian 09 program.²⁶ In order to gain more insights into nature of intermolecular interactions found within different molecular dimers identified from PIXEL energy analysis, the topological analysis was performed with the AIMALL package.²⁷ For this, the wave functions were generated from the

single point energy calculation (at crystal structure geometry with the normalized H involving distances to their typical neutron values) at the M06-2X-D3/cc-pVTZ level of theory.^{28,29} Further, to understand the preference of N-H group orientation, we performed rigid potential energy surface scan for the torsion angle S1-C3-N1-C2 in compound **I** using Jaguar program³⁰ with B3LYP functional,³¹ and 6-31G(d) basis set. The molecular electrostatic potentials were also computed with WFA-SAS program³² to identify the electrostatic complementary regions within the molecule.

Results and discussion

In the present study, we explored the role of various non-covalent interactions in three adamantane derivatives using different theoretical approaches. Two of the structures (**II** and **III**) contain halogen atoms (F and Br). Crystal data, data collection details and refinement statistics for all three compounds are presented in Table 1.

Crystal structure of **I**

Compound **I** crystallizes in the monoclinic system with the space group of $P2_1/c$ and its asymmetric unit comprises of one

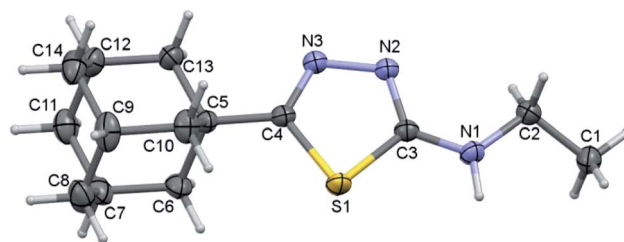


Fig. 1 Thermal ellipsoidal plot of compound **I**. The ellipsoids are drawn at the 50% probability level.

molecule (Fig. 1). Four fused cyclohexane rings constitute the adamantane moiety and each of these six-membered rings is in chair conformation as evident from the Cremer and Pople puckering parameters.³³ The orientation of the N-H group is in *syn* conformation with respect to the orientation of the S atom. Similar orientation has been observed in a closely related structure of methylamine derivative.³⁴

In order to understand the preference of *syn* conformation of amine group in the solid state, we performed a rigid potential energy surface scan (PES). The results suggest that the *syn* conformation ($S1-C3-N1-C2 = 5^\circ$) is found to be minimum energy conformer and the energy difference between *syn* and

Table 1 Crystal data and refinement parameters for compounds **I**–**III**

	I	II	III
Crystal data			
Chemical formula	$C_{14}H_{21}N_3S$	$C_{18}H_{20}FN_3S$	$C_{18}H_{20}BrN_3S$
M_r	263.40	329.43	390.34
Crystal system, space group	Monoclinic, $P2_1/c$	Triclinic, $P1$	Triclinic, $P1$
Temperature (K)	160 (2)	160 (2)	160 (2)
a, b, c (Å)	9.8339 (2), 15.8974 (2), 9.4749 (2)	6.7254 (7), 10.9787 (5), 11.9955 (10)	6.7648 (2), 11.4551 (2), 11.4985 (2)
α, β, γ (°)	90, 114.464 (2), 90	116.607 (6), 94.587 (8), 90.941 (6)	110.417 (2), 95.240 (2), 93.613 (2)
V (Å ³)	1348.26 (5)	788.01 (12)	827.26 (3)
Z	4	2	2
Radiation type	Cu K α	Cu K α	Cu K α
μ (mm ⁻¹)	2.01	1.93	4.57
Crystal size	$0.16 \times 0.14 \times 0.05$	$0.14 \times 0.05 \times 0.02$	$0.28 \times 0.11 \times 0.08$
Data collection			
Diffractionmeter	XtalLab Synergy, Dualflex, Pilatus 200 K	XtalLab Synergy, Dualflex, Pilatus 200 K	XtalLab Synergy, Dualflex, Pilatus 200 K
Absorption correction	Analytical	Analytical	Analytical
T_{min}, T_{max}	0.795, 0.902	0.851, 0.972	0.461, 0.767
No. of measured, independent and observed [$I > 2\sigma(I)$] reflections	15 881, 2920, 2798	12 473, 3183, 2735	14 178, 3385, 3269
R_{int}	0.022	0.063	0.021
$(\sin \theta/\lambda)_{max}$ (Å ⁻¹)	0.637	0.625	0.625
Refinement			
$R[F^2 > 2\sigma(F^2)], wR(F^2), S$	0.032, 0.084, 1.06	0.065, 0.203, 1.06	0.023, 0.061, 1.05
No. of reflections	2920	3183	3385
No. of parameters	168	212	212
H-atom treatment	H-atom treated by a mixture of independent and constrained refinement	H-atom treated by a mixture of independent and constrained refinement	H-atom treated by a mixture of independent and constrained refinement
$\Delta\rho_{max}, \Delta\rho_{min}$ (e Å ⁻³)	0.30, -0.31	0.40, -0.34	0.27, -0.51
CCDC no.	1977639	1977750	1977643



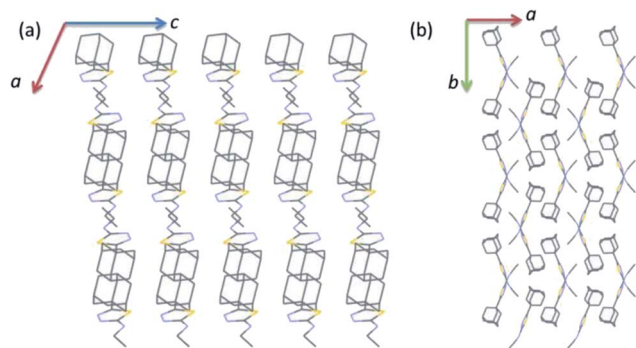


Fig. 2 Wireframe showing the crystal structure of **I** projected onto different planes (a) *ac* plane and (b) *ab* plane. All the H atoms have been omitted for clarity.

anti-conformations (180°) is being as small as $0.68 \text{ kcal mol}^{-1}$. The PES diagram for compound **I** is given in ESI (Fig. S1†).

The adamantane core and the 1,3,4-thiadiazole ring are positioned nearly co-planar (6.98°) as evident from the dihedral angle formed between the mean planes of the respective units. The ethylamine moiety makes a dihedral angle of 21.51° with respect to the mean plane of the 1,3,4-thiadiazole ring. The topological analysis for the molecule of **I** (X-ray geometry) reveals that there is no intramolecular non-covalent interaction formed.

As illustrated in Fig. 2, the crystal structure of **I** can be described as layers in which adamantane moieties from adjacent layers are positioned closer to each other. This closer arrangement is stabilized by weak and short intermolecular $\text{Csp}^3\text{-H}\cdots\text{H-Csp}^3$ type of interactions. As mentioned in the experimental section, the PIXEL energy analysis was carried out to identify the energetically significant molecular dimer in the crystalline state. In **I**, there are five molecular pairs (M1–5) identified from the PIXEL energy analysis and intermolecular interaction energies (E_{tot}) for these dimers along with their partitioned energies are presented (Table 2 and Fig. 3). It should be emphasized that the energetically least dimers (M4–5) are purely stabilized by short intermolecular $\text{Csp}^3\text{-H}\cdots\text{H-Csp}^3$ contacts. Similar adamantane–adamantane interactions (motif M4) mediated by $\text{Csp}^3\text{-H}\cdots\text{H-Csp}^3$ bonding has been reported earlier.¹¹ This interaction is named as H–H bonding and non-electrostatic nature of this closed-shell interaction have been discussed in detail.³⁵

Three intermolecular interactions ($\text{N1-H1}\cdots\text{N2}$, $\text{C1-H1B}\cdots\text{N3}$ and $\text{C2-H2A}\cdots\text{S1}$) stabilize the molecular dimer M1 (E_{tot} : $-11.5 \text{ kcal mol}^{-1}$ with 70% contribution of electrostatic energy towards stabilization). The hydrogen bonding geometry favours for the $\text{N1-H1}\cdots\text{N3}$ interaction ($\text{H1}\cdots\text{N3} = 2.40 \text{ \AA}$ and $\angle\text{N1-H1}\cdots\text{N3} = 143^\circ$). We note that the $\text{H2A}\cdots\text{S1}$ interaction is established by slightly longer (by 0.12 \AA) than the sum of the vdW radii of H and S atoms. The NCI plot and topological analysis reveals that the $\text{N1-H1}\cdots\text{N3}$ interaction is not existing and only directional intermolecular $\text{N1-H1}\cdots\text{N2}$ hydrogen bonding along with $\text{C1-H1B}\cdots\text{N3}$ and $\text{C2-H2A}\cdots\text{S1}$ interactions are formed (Fig. S2, ESI†). The second strongest molecular pair (M2; E_{tot} : $-10.5 \text{ kcal mol}^{-1}$) forms through three intermolecular $\text{C-H}\cdots\text{N}$ (involving H11B and N1), $\text{C-H}\cdots\text{Cg1}(\pi)$ (involving H6A and centroid of the five-membered ring) and a short $\text{Csp}^3\text{-H}\cdots$

H-Csp^3 type (involving H atoms of adamantane and terminal methyl groups) H–H bonding interactions. The dispersion energy contributes 66–78% towards the stabilization of this and the subsequent dimers (M3–5) observed in **I**.

Molecules of **I** which are related by center of inversion that generate a molecular dimer M3 (E_{tot} : $-5.4 \text{ kcal mol}^{-1}$). This dimer is stabilized by an intermolecular $\text{C-H}\cdots\text{N}$ (involving H14B and N3) interaction and two short $\text{H}\cdots\text{H}$ contacts (2.14 and 2.33 \AA) involving H atoms of adjacent adamantane moieties. Dimers M4 (E_{tot} : $-4.1 \text{ kcal mol}^{-1}$) and M5 (E_{tot} : $-3.2 \text{ kcal mol}^{-1}$) are generated *via* short intermolecular $\text{Csp}^3\text{-H}\cdots\text{H-Csp}^3$ type H–H bonding interactions. Adjacent adamantane moieties are interacting in M4, while adamantane and ethyl groups are interacting in M5. It is noted that the adjacent dimers of M2 are interconnected by motif M3 and this arrangement generate a sequence of motifs M2–M3–M2. The adjacent M2–M3–M2 sequences are further interlinked by motif M4 as shown in Fig. 4.

Crystal structure of the fluoro derivative **II**

The fluoro derivative **II** crystallizes in the triclinic system with the centrosymmetric $P\bar{1}$ space group and one molecule in the asymmetric unit (Fig. 5). The fused cyclohexane rings of the adamantane core exhibit chair conformation as observed in **I**. The orientation of the N–H group is in *anti*-conformation with respect to the orientation of S atom. This feature is completely different in the crystal structure of **I** and its closely related structure.³⁴ The fluoro phenyl ring makes a dihedral angle of 36.59° with the plane of the five-membered ring.

Topological analysis has been performed for X-ray geometry of **II** to identify possible intramolecular noncovalent interactions. The topological parameters and molecular graphs are presented in ESI (Table S1 and Fig. S3†). An intramolecular $\text{C-H}\cdots\text{S}$ (involving H3 and S1) interaction is existed in the molecule of **II**. The dissociation energy (D_e) for this interaction was calculated to be $2.87 \text{ kcal mol}^{-1}$ with the R_{ij} value of 2.599 \AA .

The crystal packing of **II** is completely different as compared to the crystal structure of **I**. The crystal packing can be described as hydrogen-bonded dimer mediated by $\text{N-H}\cdots\text{N}$ interaction and dimeric units packed as columnar manner along the crystallographic *b* axis (Fig. 6). In each column, the adjacent $\text{N-H}\cdots\text{N}$ mediated dimeric pairs are interlinked by intermolecular $\text{C-H}\cdots\text{F}$ interaction and π -stacking interaction between adjacent fluorophenyl rings. Further, the adamantane moiety of **II** in one column interacts with the adamantane moieties of the adjacent column *via* short intermolecular $\text{Csp}^3\text{-H}\cdots\text{H-Csp}^3$ type H–H bonding interactions.

In compound **II**, eight energetically significant molecular pairs (motifs M6–M13; see Table 2 and Fig. 7) were revealed by the PIXEL energy analysis. The intermolecular interaction energies for these molecular pairs are ranging from -21.7 to $-1.8 \text{ kcal mol}^{-1}$. These molecular dimers are stabilized by different types of non-covalent interactions such as a strong $\text{N-H}\cdots\text{N}$, several weak $\text{C-H}\cdots\text{C}(\pi)$, $\text{C-H}\cdots\text{N}$, $\text{C-H}\cdots\text{F}$, π -stacking interaction and short $\text{Csp}^3\text{-H}\cdots\text{H-Csp}^3$ type H–H bonding interactions.



Table 2 Intermolecular interaction energies (in kcal mol^{−1}) obtained by the PIXEL method for various molecular pairs observed in the crystal structures of I–III

Motif	CD	Symmetry	Important interactions	Geometry ^a (H...A, ∠D–H...A)	<i>E</i> _{coul}	<i>E</i> _{pol}	<i>E</i> _{pol}	<i>E</i> _{rep}	<i>E</i> _{tot}
Compound I									
M1	7.915	<i>x</i> , − <i>y</i> + 3/2, <i>z</i> − 1/2	N1–H1...N2 C1–H1B...N3 C2–H2A...S1	1.98, 176 2.68, 136 3.11, 131	−11.4	−5.4	−5.4	12.5	−11.5
M2	4.755	− <i>x</i> + 1, − <i>y</i> + 1, − <i>z</i> + 1	C11–H11B...N1 H11A...H1A C6–H6A...Cg1	2.63, 141 2.22, 119 2.77, 152	−5.0	−2.9	−2.9	14.1	−10.5
M3	6.831	− <i>x</i> + 2, − <i>y</i> + 1, − <i>z</i> + 2	C14–H14B...N3 H14B...H13A H10B...H13A	2.72, 140 2.14, 149 2.33, 142	−2.4	−2.0	−2.0	7.5	−5.4
M4	6.638	− <i>x</i> + 2, − <i>y</i> + 1, − <i>z</i> + 1	H10A...H8A	2.20, 152	−2.0	−1.3	−1.3	7.0	−4.1
M5	9.139	− <i>x</i> + 2, <i>y</i> − 1/2, − <i>z</i> + 3/2	H9...H2A	2.37, 165	−0.7	−0.4	−0.4	1.7	−3.2
Compound II									
M6	7.831	− <i>x</i> + 2, − <i>y</i> + 1, − <i>z</i> + 1	N1–H1...N2	1.91, 175	−26.5	−12.1	−9.4	26.4	−21.7
M7	4.947	− <i>x</i> + 1, − <i>y</i> + 1, − <i>z</i> + 1	Cg1...Cg1 C17–H17B...C4 C17–H17B...C3	3.712 (4) 2.70, 172 2.74, 157	−3.6	−2.6	−15.7	10.0	−11.8
M8	6.725	<i>x</i> − 1, <i>y</i> , <i>z</i>	C10–H10A...N2 C11–H11...C8 H11...H14B	2.72, 137 2.86, 142 2.37, 120	−1.7	−1.3	−10.3	6.4	−6.9
M9	8.488	− <i>x</i> + 1, − <i>y</i> , − <i>z</i> + 1	C10–H10B...F1	2.39, 168	−2.3	−0.8	−6.0	3.8	−5.3
M10	7.520	− <i>x</i> + 1, − <i>y</i> + 1, − <i>z</i> + 2	H14A...H14A	2.38, 123	−1.2	−0.7	−6.8	4.2	−4.6
M11	10.551	− <i>x</i> + 2, − <i>y</i> , − <i>z</i> + 1	Cg2...Cg2	3.848 (4)	−0.9	−0.4	−5.7	3.4	−3.6
M12	11.492	− <i>x</i> + 1, − <i>y</i> + 2, − <i>z</i> + 2	H16...H17A H16...H18B	2.34, 123 2.38, 123	−1.7	−0.8	−5.9	5.4	−2.9
M13	14.388	<i>x</i> − 1, <i>y</i> + 1, <i>z</i> + 1	H18A...H6	2.21, 145	−0.5	−0.4	−2.8	2.0	−1.8
Compound III									
M14	7.626	− <i>x</i> , − <i>y</i> + 2, − <i>z</i> + 1	N1–H1...N2 C5–H5...N3	1.93, 169 2.59, 149	−28.0	−13.3	−10.6	28.5	−23.4
M15	5.201	− <i>x</i> + 1, − <i>y</i> + 2, − <i>z</i> + 1	Cg1...Cg1 H6...H14B	3.687 (1) 2.27, 118	−2.3	−2.5	−19.0	14.2	−9.6
M16	8.088	− <i>x</i> , − <i>y</i> + 1, − <i>z</i> + 1	H10A...H10A C15–H15A...S1	1.93, 145 3.06, 159	−2.8	−1.9	−10.6	7.6	−7.7
M17	6.765	<i>x</i> − 1, <i>y</i> , <i>z</i>	C5–H5...Br1	3.02, 125	−2.1	−1.0	−7.2	3.2	−7.1
M18	6.639	− <i>x</i> + 1, − <i>y</i> + 1, − <i>z</i> + 1	H2...H15B H2...H11 H3...H11	2.38, 135 2.33, 106 2.18, 111	−2.7	−2.0	−11.8	9.6	−6.9
M19	11.498	<i>x</i> , <i>y</i> , <i>z</i> − 1	C13–H13...Br1	3.11, 138	−1.1	−0.4	−4.7	2.5	−3.6
M20	13.867	− <i>x</i> + 1, − <i>y</i> + 2, − <i>z</i>	C6–H6...Br1	2.92, 150	−2.1	−0.8	−3.9	3.3	−3.4
M21	16.453	− <i>x</i> , − <i>y</i> + 1, − <i>z</i> + 2	H18A...H16	2.36, 147	−0.8	−0.4	−4.3	2.7	−2.9
M22	13.863	<i>x</i> − 1, <i>y</i> , <i>z</i> + 1	C17–H17B...Br1	2.90, 145	−0.5	−0.4	−2.7	1.9	−1.8
M23	16.338	− <i>x</i> + 2, − <i>y</i> + 2, − <i>z</i>	C1–Br1...Br1	3.706 (1), 148.1 (1)	−0.6	−0.2	−1.5	1.5	−0.8

^a Neutron values are given for all D–H...A interactions. CD: centroid-to-centroid distance of the molecular pair. Cg1 and Cg2 are the centroids of the thiadiazole and phenyl rings, respectively.

The strongest dimer (M6; *E*_{tot}: −21.7 kcal mol^{−1}) in this structure is formed by an intermolecular N–H...N interaction involving amine H atom and one of the N atoms of the thiadiazole ring with R₂²(8) synthon.³⁶ This dimer is predominantly electrostatic in nature with 80% contribution towards the stabilization. The other dimers (M7–M13) found in this structure are dispersive in nature with the contribution of 66–81% towards stabilization. Dimer M7 (*E*_{tot}: −11.8 kcal mol^{−1}) forms by centrosymmetrically related molecules and stabilized by π -stacking interaction between adjacent five-membered rings and

supported by a bifurcated intermolecular C–H...C(π) interactions (involving H13B and C3/C4).

Dimer M8 (*E*_{tot}: −6.9 kcal mol^{−1}) is featured with three intermolecular interactions such as C–H...N (involving H10A and N2), C–H...C(π) (involving H11 and C8) and a short Csp³–H...H–Csp³ (involving H11 and H14B) type H–H bonding interactions. A highly directional intermolecular C–H...F interaction generates a molecular dimer M9 (*E*_{tot}: −5.3 kcal mol^{−1}). We note that the dispersion energy is nearly



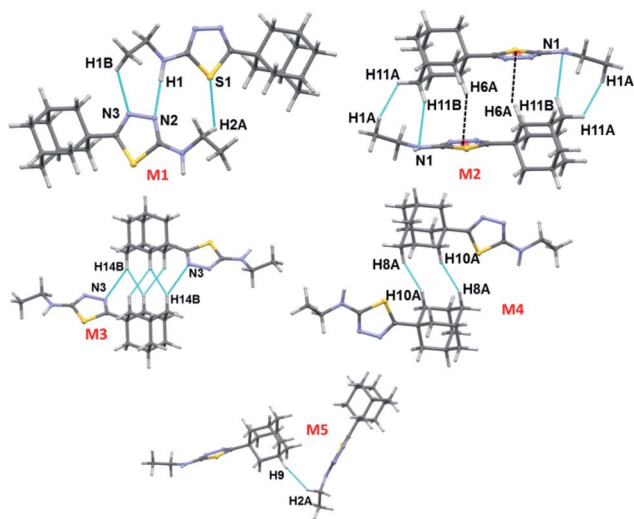


Fig. 3 Different dimeric motifs observed in crystal structure of I.

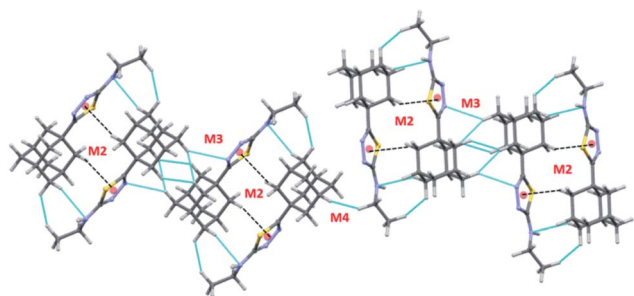


Fig. 4 Supramolecular association mediated by $\text{Csp}^3\text{-H}\cdots\text{H-Csp}^3$ type H-H bonding interactions (motifs M3 and M4) in I. Small spheres represent the centroid of the five-membered ring.

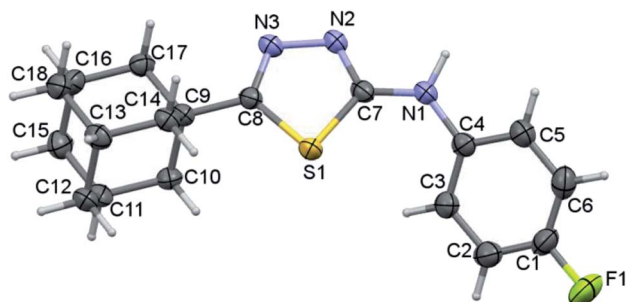


Fig. 5 Thermal ellipsoidal plot of compound II. The ellipsoids are drawn at the 50% probability level.

contributing 2 fold excess that of electrostatic energy towards the stabilization of this dimer.

In M10 dimer ($E_{\text{tot}}: -4.6 \text{ kcal mol}^{-1}$), adjacent adamantane moieties interconnected through $\text{Csp}^3\text{-H}\cdots\text{H-Csp}^3$ H-H bonding interaction. This motif helps to link the adjacent dimers formed by motif M7. The combination of motifs M7 and M10 generate a molecular ribbon which runs along the crystallographic c axis (Fig. S4, ESI†). The fluorophenyl rings are

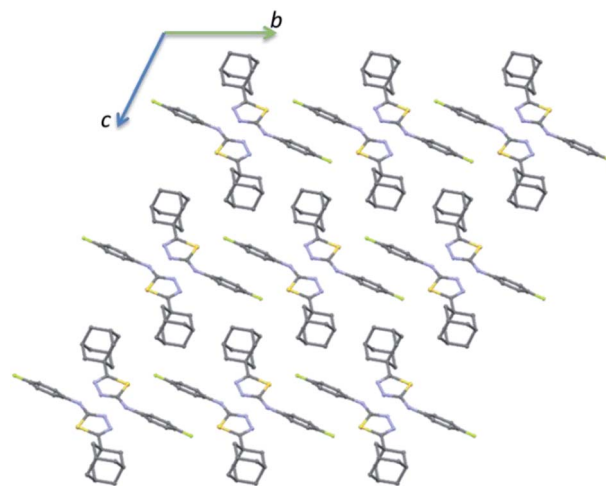


Fig. 6 Ball and stick diagram showing the crystal structure of II viewed down the a axis and all the H atoms have been omitted for clarity.

stacked against each other with the centroid-to-centroid distance of 3.848 Å in M11 ($E_{\text{tot}}: -3.6 \text{ kcal mol}^{-1}$). This stacking interaction is emanated from two adjacent dimers of M1.

Dimer M12 ($E_{\text{tot}}: -2.9 \text{ kcal mol}^{-1}$) stabilizes by short and three centered $\text{Csp}^3\text{-H}\cdots\text{H-Csp}^3$ (involving H16 and H17A/H18B) H-H bonding interactions in which two adjacent adamantane moieties are participated. Further, the neighbouring dimers formed by M9 interlinked by motif M12 as shown in Fig. 7. The least dimer M13 ($E_{\text{tot}}: -1.8 \text{ kcal mol}^{-1}$) in II also stabilizes with H-H bonding interaction (involving H18A and H6) with $\text{Csp}^3\text{-H}\cdots\text{H-Csp}^2$ type. It is of interest to note that the motifs M6, M9, M12 and M13 generate a molecular sheet as shown in Fig. 8.

Crystal structure of the bromo derivative III

The bromo derivative III crystallizes in the triclinic system with the centrosymmetric $P\bar{1}$ space group and one molecule in the asymmetric unit (Fig. 9). The conformation of the fused cyclohexane rings and the orientation of the N-H group are very similar to that of the structure of II. The bromophenyl ring is

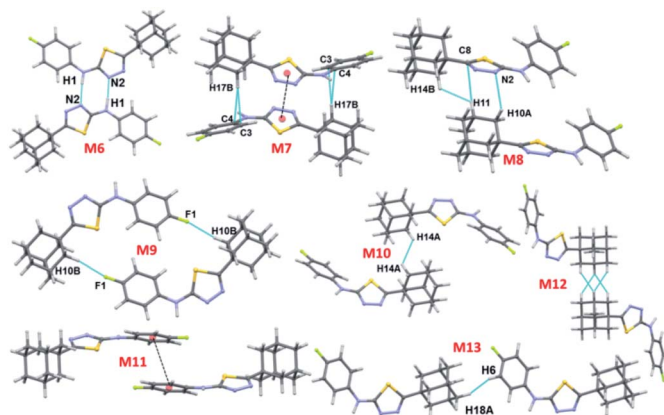


Fig. 7 Molecular pairs formed by different intermolecular interactions in II.

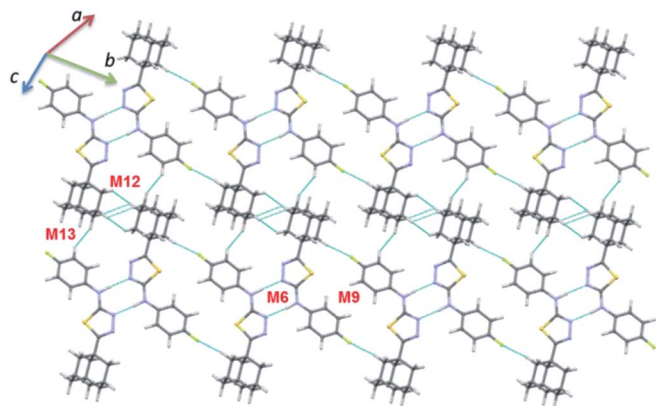


Fig. 8 Supramolecular sheet constructed by motifs M6, M9, M12 and M13 in **II**.

less twisted as compared to fluorophenyl ring in **II** with respect to the mean plane of the five-membered ring. The dihedral angle between bromophenyl and five-membered ring is being 11.13° .

The QTAIM analysis reveals that the conformation of molecule **III** is stabilized by an intramolecular C–H \cdots S interaction. Moreover, the bond path distance (2.439 Å) is quite shorter for an intramolecular C–H \cdots S interaction as compared to **II**. The dissociation energy (D_e) for this interaction was computed to be $3.63 \text{ kcal mol}^{-1}$. The molecular graph and topological parameters are presented in ESI (Table S2 and Fig. S5†).

The crystal structure of the bromo derivative is stabilized by intermolecular N–H \cdots N, C–H \cdots N, C–H \cdots Br, C–H \cdots S, π -stacking, short Csp²–H \cdots H–Csp³ and Csp³–H \cdots H–Csp³ types of H–H bonding and a Br \cdots Br contact. The crystal packing of **III** is somewhat similar to that of **II**. The basic motif can be described as a hydrogen-bonded dimer formed by N–H \cdots N and C–H \cdots N interactions and this motif arranged as columnar fashion along the crystallographic *b* axis (Fig. 10).

There are ten molecular dimers (M14–M23; see Fig. 11 and 12) brought out from the crystal structure with the PIXEL energy analysis. The intermolecular interaction energies (E_{tot}) for these dimers range from -23.4 to $-0.8 \text{ kcal mol}^{-1}$. The strongest dimer is formed by intermolecular N–H \cdots N (involving H1 and N2) and C–H \cdots N (involving H5 and N3) interactions (motif M14, E_{tot} : $-23.4 \text{ kcal mol}^{-1}$). This strong dimer is electrostatic in

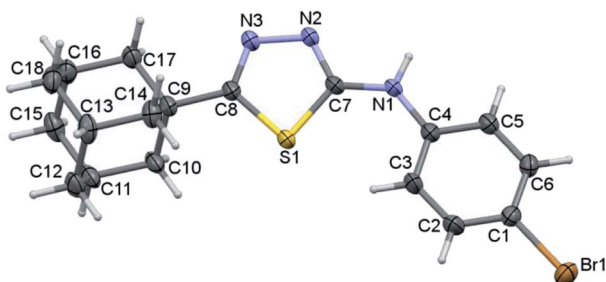


Fig. 9 Thermal ellipsoidal plot of compound **III**. The ellipsoids are drawn at the 50% probability level.

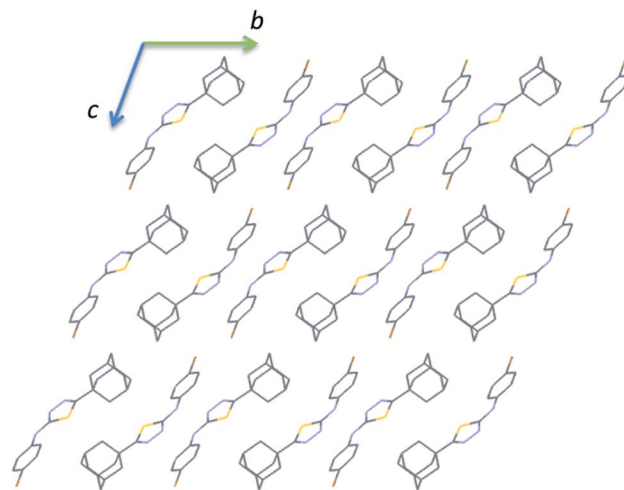


Fig. 10 Crystal packing of **III** viewed down the *a* axis. All the H atoms have been omitted for clarity.

nature with the electrostatic energy contribution of 80%. The other dimers in this structure except dimer M20 are dispersive in nature with the dispersion contribution ranging from 65–80% towards the stabilization of these dimers. In the case of dimer M20 stabilization, the contribution of electrostatic and dispersion energies are 43 and 57%, respectively. We note that the way adjacent M14 dimers are interconnected is different as compared to the structure of **II**. The adjacent M14 dimers are associated *via* Csp²–H \cdots H–Csp³ type of H–H bonding interactions (motif M18; Fig. S6, ESI†). In motif M18, the H atoms of phenyl and adamantane moieties are involved in the H–H bonding interactions with the separation of H \cdots H atoms are ranging from 2.18 to 2.36 Å.

Molecules related by center of inversion form a molecular stacking (motif M15, E_{tot} : $-9.6 \text{ kcal mol}^{-1}$) in which five-

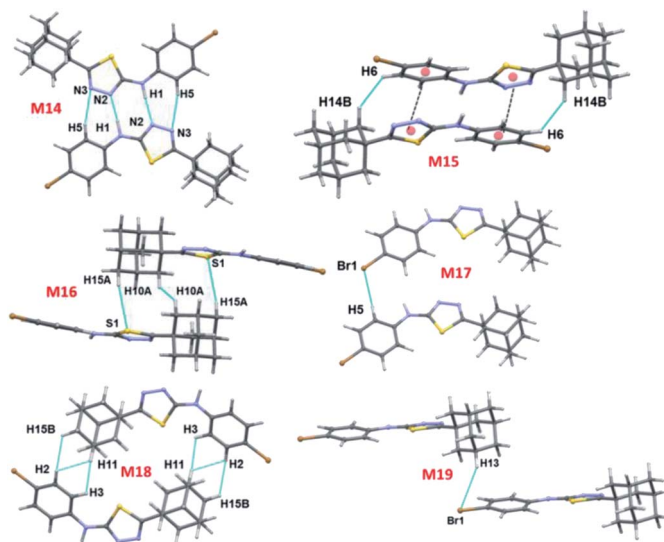


Fig. 11 Molecular pairs formed by different intermolecular interactions in **III**.



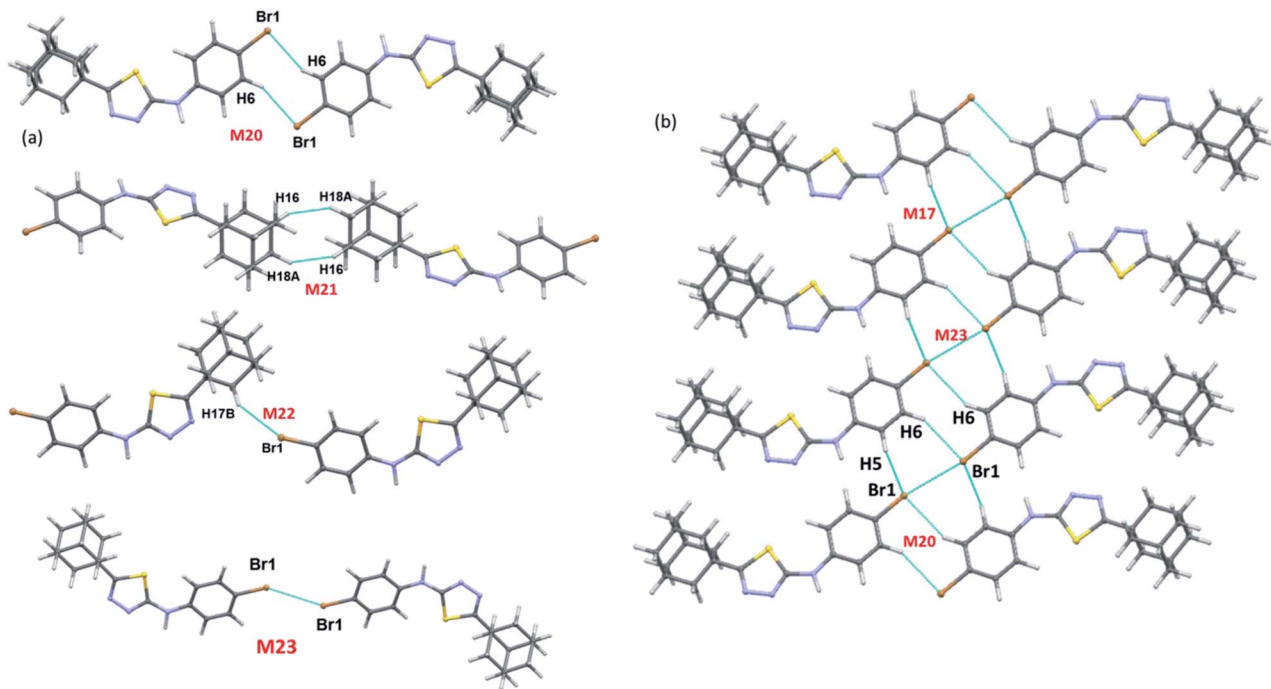


Fig. 12 (a) Molecular pairs formed by different intermolecular interactions and (b) molecular sheet formed by intermolecular C-H...Br and Csp²-Br...Br-Csp² interactions in III.

membered ring stacking against bromophenyl ring. The molecular π -stacking arrangement is further supported by intermolecular H-H bonding with a short distance of 2.27 Å. The adjacent M15 dimers are interlinked *via* intermolecular H-H bonding interactions in which the neighbouring adamantane moieties are involved (motif M21).

In motif M16 (E_{tot} : $-7.7 \text{ kcal mol}^{-1}$), adamantane moiety of one molecule interacts with the adamantane moiety of the centrosymmetrically related molecule *via* Csp³-H...H-Csp³ type of H-H bonding interaction with a very short contact distance of 1.93 Å. This dimer is further supported by a weak intermolecular C-H...S interaction (involving H15A and S1). It should be noted that the H...S distance is slightly longer than (by 0.07 Å) the sum of the van der Waals radii of the interacting atoms.

Four intermolecular C-H...Br interactions (motifs M17, M19, M20 and M22) observed in the crystal structure of bromo

derivative. The intermolecular interaction energies for these dimers are as strong as $-7.1 \text{ kcal mol}^{-1}$ and as weak as $-1.8 \text{ kcal mol}^{-1}$. The phenyl protons are acting as donors for two of the C-H...Br interactions and the protons of the adamantane moiety acts as donors for the other two interactions. We note that the H...Br contact in motif M19 is slightly longer (by 0.06 Å) than the sum of vdW radii of interacting atoms and the corresponding contacts in other motifs are formed less than the sum of vdW. The least dimeric motif (M23, E_{tot} : $-0.8 \text{ kcal mol}^{-1}$) forms by intermolecular Csp²-Br...Br-Csp² contact and this interaction is classified as type I (*trans*-geometry) contact.³⁷ As shown in Fig. 12(b), supramolecular sheet forms by Csp²-Br...Br-Csp² and two C-H...Br interactions.

To grasp the geometrical choices of homo-halogen contact (Br...Br), we carried out a CSD search (CSD version 5.40, November 2018) with conditions along with the inter-contact

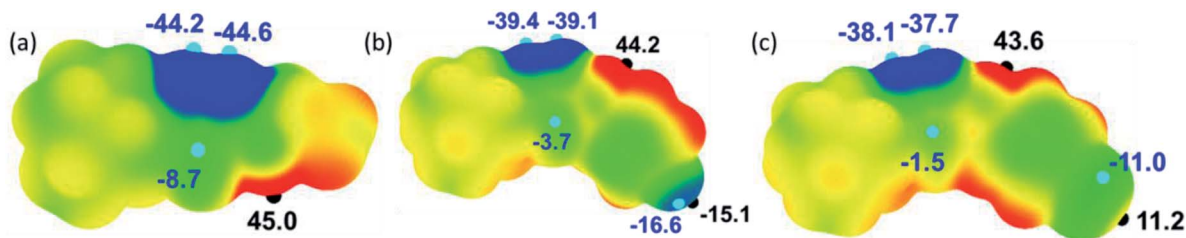


Fig. 13 Molecular electrostatic potential surfaces of the structures (a) I, (b) II and (c) III mapped over the electronic density at 0.001 au contour. Colour ranges (in kcal mol⁻¹): red: greater than 15; yellow: between 15 and 0; green: between 0 and -15 and blue: greater than -15. Important $V_{s,\text{max}}$ and $V_{s,\text{min}}$ values are given along with small hemispheres.



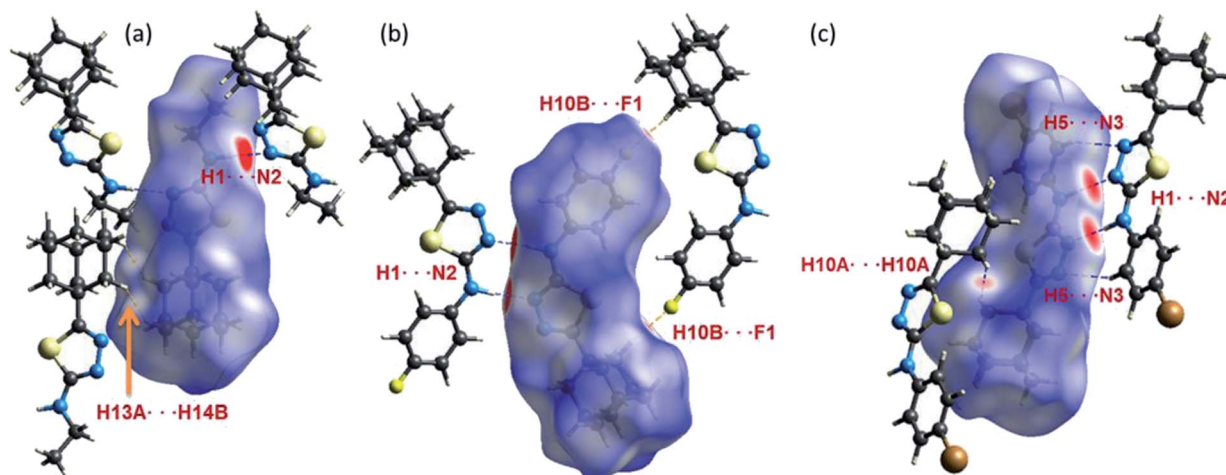


Fig. 14 Hirshfeld surfaces highlight the close inter-contacts observed in structures (a) I, (b) II and (c) III.

between Br atoms is less than the sum of van der Waals radii (3.7 Å).³⁸ This search yielded 947 hits with 1147 contacts and the minimum and average Br...Br distance are found to be 3.241 and 3.575 Å, respectively. Further analysis suggests that 39% of the contacts show type I [C-Br...Br (θ_1); Br...Br-C (θ_2) and $\theta_1 = \theta_2$] geometry and these contacts are located on the diagonal. It should be noted that 51% of the contacts display quasi type I geometry ($|\theta_1 - \theta_2| < 20^\circ$). The remaining contacts (10%) belong to type II geometry ($\theta_1 \cong 90^\circ$; $\theta_2 \cong 180$ or $\theta_1 \cong 180$; $\theta_2 \cong 90^\circ$). The scatterplots of Br...Br distance and two angles (θ_1 and θ_2) are given in ESI (Fig. S7†). This is undoubtedly revealed that the Br...Br contact has more tendency to adopt type I geometry as observed in **III**.

It is noted that the unit cell dimensions are comparable for structures **II** and **III**. To delineate the isostructurality between **II** and **III**, we calculated the isostructurality index (Π) for these structures as described by Fábrián and Kálmán³⁹ and the Π value is found to be zero. This value suggests that they are isostructural. To gain more information on the degree of packing similarity, we utilized XPac program.⁴⁰ The XPac analysis reveals that these two structures display 1D supramolecular construct (row of molecules match) as shown in ESI (Fig. S8†). The dissimilarity index (x) was calculated to be 11.2 and this parameter quantifies the deviation between these structures from perfect geometrical similarity. The stretch parameter (D) gives information on the change in the intermolecular distance between two structures. This value is calculated to be 0.42 Å for these structures.

Molecular electrostatic potential surface map

The molecular electrostatic potential surface map (MESP) has been extensively used to analyze noncovalent interactions and to identify electrophilic/nucleophilic sites on the molecule.⁴¹ The electrostatic potential mapped over the electronic density isosurface of the molecule at 0.001 au. The most positive ($V_{s,max}$) and negative potentials ($V_{s,min}$) are highlighted with small hemispheres along with values (Fig. 13). In all three structures, the amine H shows the most positive potentials in the range 42–

45 kcal mol⁻¹ and this feature indicating that the amine proton has best donating tendencies as compared to other protons in the molecule. Similarly, the most negative potentials are observed for N atoms of the thiadiazole ring. The $V_{s,min}$ values for these atoms are slightly higher in **I** as compared to **II** and **III**. We also note that the accepting tendency for S atom is in the order of **I** > **II** > **III**.

The fluoro and bromo derivatives show interesting features as can be seen from the Fig. 13. In the fluoro derivative, there is a σ -hole along C1-F1 bond in which the outermost region of its surface,⁴² with the $V_{s,max}$ value of -15.1 kcal mol⁻¹ and the unshared electrons on the F atom form negative potentials around its central portion with the $V_{s,min}$ value of -16.6 kcal mol⁻¹. A strong $V_{s,max}$ value on the outermost region of C-F bond facilitates a directional non-covalent bonding. In contrast, the outermost portion of the C-Br surface has a positive potential with $V_{s,max}$ value of 11.2 kcal mol⁻¹. The central part of this bond constitutes negative potentials with the $V_{s,min}$ value of -11.0 kcal mol⁻¹. The negative potential corresponds to the lone-pair electrons of Br atom. The MESP and PIXEL energy analysis collectively suggest

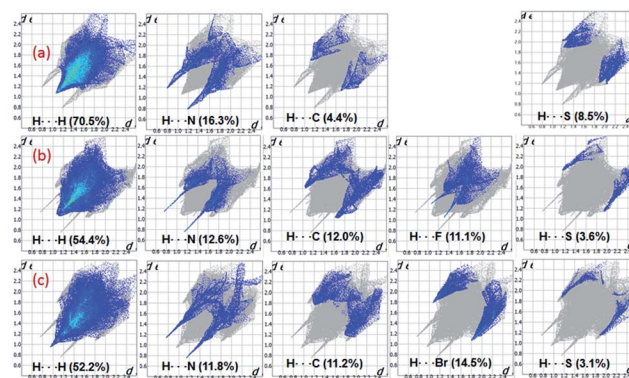


Fig. 15 2D-fingerprint plots for structures (a) I (b) II and (c) III. The percentage relative contributions of different intermolecular contacts are given.



Table 3 Topological parameters for intermolecular interactions in selected molecular pairs of I [$\rho(r)$: electron density ($\text{e } \text{\AA}^{-3}$), $\nabla^2\rho(r)$: Laplacian of electron density ($\text{e } \text{\AA}^{-5}$); $V(r)$: potential energy density, $G(r)$: kinetic energy density; $H(r)$: total energy density; R_{ij} : bond path (\AA), $D_e = -0.5 \times V(r)$ in kcal mol^{-1} and the values of $V(r)$, $G(r)$ and $H(r)$ are expressed in $\text{kJ mol}^{-1} \text{bohr}^{-3}$]

Interaction	R_{ij}	$\Delta r_D - \Delta r_A$	$\Delta r_D + \Delta r_A$	$\rho(r)$	$\nabla^2\rho(r)$	$V(r)$	$G(r)$	$H(r)$	D_e
M1									
N1–H1...N2	2.010	0.243	0.769	0.173	1.949	−55.1	54.1	−1.0	6.6
C1–H1B...N3	2.712	0.157	0.065	0.049	0.555	−9.4	12.3	2.9	1.1
C2–H2A...S1	3.142	0.108	−0.116	0.034	0.364	−5.6	7.8	2.2	0.7
M2									
C11–H11B...N1	2.643	0.172	0.124	0.060	0.695	−12.6	15.8	3.2	1.5
H11A...H1A	2.291			0.052	0.590	−10.6	−13.3	2.7	1.3
M3									
C14–H14B...N3	2.741	0.154	0.034	0.046	0.512	−8.7	11.3	2.6	1.0
H14B...H13A	2.171			0.053	0.568	−10.8	13.2	2.3	1.3
H10B...H13A	2.368			0.038	0.393	−7.2	8.9	1.8	0.9
M4									
H10A...H8A	2.229			0.048	0.500	−9.4	11.5	2.1	1.1
M5									
H9...H2A	2.410			0.032	0.359	−6.3	8.0	1.8	0.7

that the Br atom is preferred to interact with both electrophilic (positive site) and nucleophilic (negative site) sites.

Qualitative analysis of intermolecular interactions with Hirshfeld surface (HS) and 2D fingerprint plots (2D-FP)

As can be seen from the HS diagram (Fig. 14), the intermolecular H1...N2 contact (motif M1) is shown as intense and

wide red spots on the HS, whereas a small red spots appeared for intermolecular H13A...H14B contact (motif M3) in **I**. In **II**, three intermolecular short contacts (H1...N2, H10B...F1 and H7A...C3/C4) are visible on the HS. In **III**, the motif M13, comprises two intermolecular contacts (involving H1 and N2 and H5 and N3) is visible on the HS. The former contact is very short and shown as bright red areas, while the latter is shown as a paint red spots. It should be noted that

Table 4 Topological parameters for intermolecular interactions in selected molecular pairs of II [$\rho(r)$: electron density ($\text{e } \text{\AA}^{-3}$), $\nabla^2\rho(r)$: Laplacian of electron density ($\text{e } \text{\AA}^{-5}$); $V(r)$: potential energy density, $G(r)$: kinetic energy density; $H(r)$: total energy density; R_{ij} : bond path (\AA), $D_e = -0.5 \times V(r)$ in kcal mol^{-1} and the values of $V(r)$, $G(r)$ and $H(r)$ are expressed in $\text{kJ mol}^{-1} \text{bohr}^{-3}$]

Interaction	R_{ij}	$\Delta r_D - \Delta r_A$	$\Delta r_D + \Delta r_A$	$\rho(r)$	$\nabla^2\rho(r)$	$V(r)$	$G(r)$	$H(r)$	D_e
M6									
N1–H1...N2	1.943	0.274	0.832	0.220	1.922	−70.3	61.3	−9.0	8.4
M7									
C17–H17B...C4	3.133	0.125	0.151	0.053	0.611	−10.5	13.6	3.1	1.3
M8									
C10–H10A...N2	2.753	0.157	0.021	0.047	0.532	−9.1	11.8	2.7	1.1
C11–H11...C8	2.912	0.031	0.031	0.040	0.450	−8.2	10.2	2.0	1.0
H11...H14B	2.429			0.041	0.453	−8.2	10.3	2.1	1.0
M9									
C10–H10B...F1	2.406	0.069	0.281	0.052	0.811	−13.8	17.9	4.1	1.6
M10									
H14A...H14A	2.427			0.040	0.437	−8.0	10.0	2.0	1.0
M12									
H16...H17A	2.405			0.040	0.433	−8.0	9.9	1.9	1.0
H16...H18B	2.441			0.038	0.412	−7.5	9.4	1.8	0.9
M13									
H18A...H6	2.279			0.051	0.563	−10.2	12.8	2.6	1.2



intermolecular $\text{Csp}^3\text{-H10A}\cdots\text{H10A-Csp}^3$ (motif M15) type H-H bonding is also identified on the HS with red spots.

The fingerprint plots are used to delineate the relative contribution of different intermolecular contacts (Fig. 15). In all three structures, the $\text{H}\cdots\text{H}$ contacts constitute significant amount of interactions of the total HS area ranging from 52.2 to 70.5%. The shortest intermolecular $\text{H}\cdots\text{N}$ contacts are located near 2.0 Å with double spikes in all three structures. Further, there is a reduction in the relative contribution of $\text{H}\cdots\text{C/C}\cdots\text{H}$ contacts which represent intermolecular $\text{C-H}\cdots\text{C}(\pi)$ interaction and a slight increase of $\text{H}\cdots\text{S}$ interaction in **I** as compared to **II** and **III**. The feature of $\text{H}\cdots\text{S}$ interaction is in good agreement with the MESP. Moreover, the reduction of $\text{H}\cdots\text{C}$ contacts is largely compensated by intermolecular $\text{H}\cdots\text{H}$ interactions.

The relative contributions of different intermolecular contacts are comparable in the bromo and fluoro derivatives. However, a noticeable difference is observed for the distribution of these contacts on the fingerprint plots. For instance, the $\text{H}\cdots\text{H}$ contacts are appeared as a sharp spike with the shortest distance is located around 1.9 Å in **III**, while the corresponding contacts are showed blunt end towards the shortest contacting region which is closer to 2.2 Å in **II**.

Another remarkable difference is noticed for $\text{H}\cdots\text{X}$ ($\text{X} = \text{Br}$ and F) contacts and the shortest $\text{H}\cdots\text{F}$ and $\text{H}\cdots\text{Br}$ contacts are located near 2.4 and 2.9 Å, respectively. The relative contribution of $\text{H}\cdots\text{Br}$ is slightly higher (3.4%) as compared to the contribution of $\text{H}\cdots\text{F}$. According to the PIXEL energy analysis, the Br atom is involved as an acceptor in four different motifs, whereas the F atom is involved in only motif. Overall, the shortest distances of $\text{H}\cdots\text{X}$ contacts and their relative contributions in the respective structure are in good agreement with the PIXEL energy analysis. The intermolecular $\text{C}\cdots\text{C}$ contacts contribute only 2% to the total HS area in **II** and **III**, no such contact is observed in **I**. We observe that the $\text{Br}\cdots\text{Br}$ contact contributes only about 0.9% to the total HS area.

QTAIM analysis

The topological parameters are computed for different non-covalent interactions at their point critical points (BCPs) in selected dimeric pairs of **I-III** to evaluate their nature and strength (Tables 3–5). The molecular graphs of selected molecular dimers featuring various noncovalent interactions at the bond critical points are given in ESI (Fig. S9–S11†). For the evaluation of intermolecular interactions, the first four criteria [(i) bond critical point (ii) electron density $\rho(r)$, (iii) the

Table 5 Topological parameters for intermolecular interactions in selected molecular pairs of **III** [$\rho(r)$: electron density ($\text{e}\text{Å}^{-3}$), $\nabla^2\rho(r)$: Laplacian of electron density ($\text{e}\text{Å}^{-5}$); $V(r)$: potential energy density, $G(r)$: kinetic energy density; $H(r)$: total energy density; R_{ij} : bond path (Å), $D_e = -0.5 \times V(r)$ in kcal mol^{-1} and the values of $V(r)$, $G(r)$ and $H(r)$ are expressed in $\text{kJ mol}^{-1} \text{bohr}^{-3}$]

Interaction	R_{ij}	$\Delta r_D - \Delta r_A$	$\Delta r_D + \Delta r_A$	$\rho(r)$	$\nabla^2\rho(r)$	$V(r)$	$G(r)$	$H(r)$	D_e
M14									
N1–H1 \cdots N2	1.953	0.275	0.821	0.217	1.912	−68.6	60.4	−8.3	8.2
C5–H5 \cdots N3	2.620	0.172	0.156	0.051	0.650	−10.6	14.2	3.6	1.3
M15									
H6 \cdots H14B	2.383			0.048	0.543	−9.4	12.1	2.7	1.1
M16									
H10A \cdots H10A	1.963			0.082	0.920	−17.9	21.5	3.6	2.1
C15–H15A \cdots S1	3.078	0.149	−0.061	0.039	0.391	−6.6	8.6	2.0	0.8
M17									
C5–H5 \cdots Br1	3.064	0.119	0.023	0.049	0.520	−9.0	11.6	2.6	1.1
M18									
H3 \cdots H11	2.316			0.056	0.659	−12.2	15.1	2.9	1.5
H2 \cdots H11	2.530			0.049	0.608	−10.7	13.6	2.9	1.3
H2 \cdots H15B	2.487			0.038	0.452	−7.7	10.0	2.3	0.9
M19									
C13–H13 \cdots Br1	3.128	0.119	−0.059	0.039	0.430	−7.4	9.6	2.1	0.9
M20									
C6–H6 \cdots Br1	2.942	0.185	0.125	0.053	0.552	−9.9	12.5	2.6	1.2
M21									
H18A \cdots H16	2.400			0.037	0.395	−7.2	9.0	1.8	0.9
M22									
C17–H17B \cdots Br1	2.926	0.073	0.145	0.050	0.555	−9.9	12.5	2.6	1.2



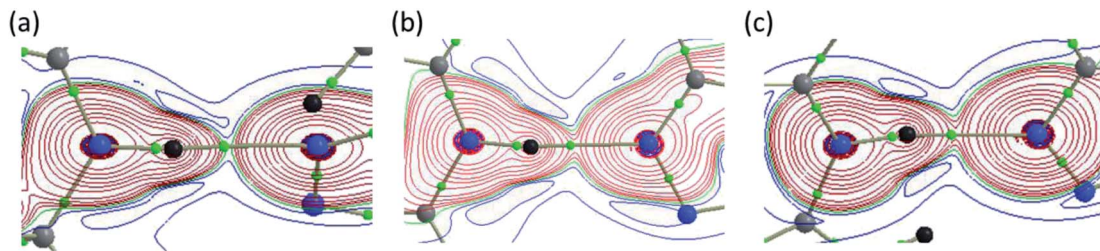


Fig. 16 Total electronic density distribution $H(r)$ showing the formation of strong intermolecular N–H...N hydrogen bonds in (a) I, (b) II and (c) III. All the plots are drawn in the plane comprising the atoms involved in the hydrogen bond and small green spheres represent the bond critical points.

Laplacian of electron density $\nabla^2\rho(r)$ and mutual penetration of the H and the acceptor atom] of KP are used.⁴³ It is worthy to note that the H–H bonding is characterized using the first 3 criteria of KP.

In **I**, one N–H...N and three C–H...N, one C–H...S, one C–H...C and five $\text{Csp}^3\text{--H}\cdots\text{H}\cdots\text{Csp}^3$ type H–H bonding interactions were observed. The bond critical points (BCPs) are clearly detected and confirmed the existence of these interactions except C–H...C(π) interaction. The $\rho(r)$ values for these interactions lie in the range $0.032\text{--}0.173\text{ e \AA}^{-3}$ and these values satisfy the KP limit [$0.013 < \rho(r) \text{ e \AA}^{-3} < 0.236$] for hydrogen bonds. It is interesting to convey that only three intermolecular interactions (N1–H1...N2, C11–H11B...N1 and $\text{Csp}^3\text{--H11A}\cdots\text{H1A}\cdots\text{Csp}^3$ type H–H bonding) are in agreement with the suggested values [$0.580 < \nabla^2\rho(r) \text{ e \AA}^{-5} < 3.355$] of KP. The KP-4 rule is found to be extremely important to differentiate the classical hydrogen bonds from van der Waals interactions. As shown in Table 3, all the classical intermolecular interactions showing hydrogen bonding character except C–H...S interaction.

The dissociation energies for these interactions are in the range of 0.7 to 6.6 kcal mol^{-1} . Among these interactions, the intermolecular N1–H1...N2 (motif M1) hydrogen bond has a negative total electronic density $H(r)$ value of $-1.0\text{ kJ mol}^{-1}\text{ b}^{-3}$. The positive value of Laplacian and $H(r) < 0$ indicate that the N–H...N interaction shows the intermediate bonding character between shared and closed shell interaction.⁴⁴ The remaining interactions including H–H bonding are closed shell in nature as they obey the positive value of Laplacian and $H(r) > 0$. The results clearly demonstrate that the H–H bonding interactions also play significant roles in the crystalline state of **I**.

In **II**, the dissociation energies for intermolecular interactions are in the range of $0.9\text{--}8.4\text{ kcal mol}^{-1}$ (Table 4). The D_e value for $\text{Csp}^3\text{--H}\cdots\text{H}\cdots\text{Csp}^3$ and $\text{Csp}^3\text{--H}\cdots\text{H}\cdots\text{Csp}^2$ interactions are found to be $0.9\text{--}1.2\text{ kcal mol}^{-1}$. The $\rho(r)$ values for intermolecular interactions noted in **II** fulfil the KP limit. However, only three intermolecular interactions (N1–H1...N2, C17–H17B...C4 and C10–H10B...F1) are obeyed the proposed KP limit for the Laplacian of the electron density. The positive value of Laplacian, $H(r) > 0$ and $\frac{V(r)}{G(r)} < 1$ for the H–H bonding suggest that they are closed shell in nature. The remaining interactions are classified as hydrogen bond on the basis of KP-4 rule. It

should be noted that the positive value of the Laplacian of electron density, $H(r) < 0$ and $\frac{V(r)}{G(r)} > 1$ reveal that intermolecular N1–H1...N2 interaction is found to be intermediate bonding nature between shared and closed shell interaction as similar to the motif I. We note that the intermolecular C–H...F and C–H...C(π) interactions are found to be stronger after N–H...N hydrogen bond based on the $H(r)$ values.

In **III**, the Laplacian of the electron density values for intermolecular N–H...N and C–H...N interactions comply with the proposed values for hydrogen bonds. The KP-4 rule suggests that N–H...N, C–H...N and three C–H...Br (out of four) interactions are showing hydrogen bonding character. The H–H bonding interactions in this structure are closed shell in nature. The distribution of total electronic energy density $H(r)$ is shown in Fig. 16 for intermolecular N–H...N hydrogen bond in all three structures. From this figure one can see the transit region (between shared and closed shell nature) for N–H...N hydrogen bond in **II** and **III**. In **III**, the stronger interaction is found to be N–H...N followed by C–H...N, H–H bonding and C–H...Br interactions in regard to the $H(r)$ values. The analysis of topological properties for these interactions apparently supports the importance of weak nature of non-classical H–H bonding interactions.

Conclusions

In the present investigation, three pharmaceutically promising adamantane–thiadiazole hybrid derivatives have been synthesized and their crystal structures at low temperature have been determined. The orientation of the amino group was completely different between halophenylamino and ethylamino derivatives. This feature was not favoured for the formation of a $R_2^2(8)$ synthon in **I**. Crystal structures of **II** and **III** showed isostructural behaviour with 1D supramolecular construct. Further, different theoretical tools were used to characterize the noncovalent interactions present in these compounds. Hirshfeld surface analysis revealed that the halogenated compounds showed similar relative contributions of different intermolecular interactions, whereas ethylamino derivative showed variations in the relative contributions of H...H and H...C and H...S contacts as compared to halogenated derivatives. Topological analysis was performed for selected dimeric pairs of these



compounds. The first four criteria of KP have been used to characterize the nature and strength of noncovalent interactions. The results indicate that there was a strong N-H...N hydrogen bond formed between amino group and one of the N atoms of the thiadiazole ring. The strength of this interaction was found to be relatively weaker in **I** as compared to **II** and **III**. The molecular electrostatic potential surface map suggested that the S atom showed weaker accepting tendencies in varying degrees and participated in van der Waals interactions. The intermolecular C-H...N, C-H...F and C-H...Br and C-H...C(π) showed hydrogen bonding character and H-H bonding interactions displayed weak and closed shell in nature.

Conflicts of interest

The authors declare that they have no competing interests.

Acknowledgements

This work was funded by the Deanship of Scientific Research at Princess Nourah bint Abdulrahman University through the Research Group Program (Grant No. RGP-1438-0010). ST thanks the DST-SERB (SB/YS/LS-19/2014) for financial support. ST and MJP would like to thank Laboratorio Nacional de Supercomputo del Sureste (LNS-BUAP) for computational resource.

References

- (a) Y. Hu, C.-Y. Li, X.-M. Wang, Y.-H. Yang and H.-L. Zhu, *Chem. Rev.*, 2014, **114**, 5572–5610; (b) A. K. Jain, S. Sharma, A. Vaidya, V. Ravichandran and R. K. Agrawal, *Chem. Biol. Drug Des.*, 2013, **81**, 557–576.
- C. T. Supuran, *Nat. Rev. Drug Discovery*, 2008, **7**, 168–181.
- (a) A. A. Kadi, E. S. Al-Abdullah, I. A. Shehata, E. E. Habib, T. M. Ibrahim and A. A. El-Emam, *Eur. J. Med. Chem.*, 2010, **45**, 5006–5011; (b) R. J. Fosbinder and L. A. Walter, *J. Am. Chem. Soc.*, 1939, **61**, 2032–2033; (c) P. Li, L. Shi, M.-N. Gao, X. Yang, W. Xue, L.-H. Jin, D.-Y. Hu and B.-A. Song, *Bioorg. Med. Chem. Lett.*, 2015, **25**, 481–484; (d) P. Zhou, X. Mo, W. Wang, X. Chen and Y. Lou, *Int. J. Mol. Sci.*, 2018, **19**, 1271.
- (a) Z.-N. Cui, Y.-S. Li, D.-K. Hu, H. Tian, J.-Z. Jiang, Y. Wang and X.-J. Yan, *Sci. Rep.*, 2016, **6**, 20204; (b) Y. Li, J. Geng, Y. Liu, S. Yu and G. Zhao, *ChemMedChem*, 2013, **8**, 27–41.
- (a) H. J. Khoury, G. Garcia-Manero, G. Borthakur, T. Kadia, M. C. Foudray, M. Arellano, A. Langston, B. Bethelmie-Bryan, S. Rush, K. Litwiler, S. Karan, H. Simmons, A. I. Marcus, M. Ptaszynski and H. Kantarjian, *Cancer*, 2012, **118**, 3556–3564; (b) D. M. Altıntop, I. H. Ciftci, O. M. Radwan, B. Sever, A. Z. Kaplancikli, F. S. T. Ali, R. Koga, M. Fujita, M. Otsuka and A. Özdemir, *Molecules*, 2018, **23**, 59.
- X. Gan, D. Hu, Z. Chen, Y. Wang and B. Song, *Bioorg. Med. Chem. Lett.*, 2017, **27**, 4298–4301.
- K. Salomão, E. M. de Souza, S. A. Carvalho, E. F. da Silva, C. A. M. Fraga, H. S. Barbosa and S. L. de Castro, *Antimicrob. Agents Chemother.*, 2010, **54**, 2023–2031.
- G. Serban, *Molecules*, 2019, **24**, 1557.
- (a) J. Liu, D. Obando, V. Liao, T. Lifa and R. Codd, *Eur. J. Med. Chem.*, 2011, **46**, 1949–1963; (b) L. Guy and A. Graciela, *Curr. Med. Chem.*, 2010, **17**, 2967–2978.
- L. Wanka, K. Iqbal and P. R. Schreiner, *Chem. Rev.*, 2013, **113**, 3516–3604.
- (a) L. H. Al-Wahaibi, S. Sujay, G. G. Muthu, A. A. El-Emam, N. S. Venkataramanan, F. A. M. Al-Omary, H. A. Ghabbour, J. Percino and S. Thamotharan, *J. Mol. Struct.*, 2018, **1159**, 233–245; (b) H. L. Al-Wahaibi, M. H. Hassan, M. A. Abo-Kamar, A. H. Ghabbour and A. A. El-Emam, *Molecules*, 2017, **22**, 710; (c) L. H. Al-Wahaibi, J. Joubert, O. Blacque, N. H. Al-Shaalan and A. A. El-Emam, *Sci. Rep.*, 2019, **9**, 19745.
- M. A. Spackman and D. Jayatilaka, *CrystEngComm*, 2009, **11**, 19–32.
- (a) A. Gavezzotti, *J. Phys. Chem. B*, 2003, **107**, 2344–2353; (b) A. Gavezzotti, *Mol. Phys.*, 2008, **106**, 1473–1485; (c) A. Gavezzotti, *New J. Chem.*, 2011, **35**, 1360–1368; (d) A. Gavezzotti, *J. Phys. Chem. B*, 2002, **106**, 4145–4154.
- R. Bader, *Atoms in Molecules: A Quantum Theory*, Oxford University Press, USA, 1994.
- U. Koch and P. L. A. Popelier, *J. Phys. Chem. B*, 1995, **99**, 9747–9754.
- (a) A. Bondi, *J. Phys. Chem.*, 1964, **68**, 441–451; (b) S. C. Nyburg and C. H. Faerman, *Acta Crystallogr., Sect. B: Struct. Sci.*, 1985, **41**, 274–279.
- (a) P. Munshi and T. N. Guru Row, *Cryst. Growth Des.*, 2006, **6**, 708–718; (b) P. Munshi, C. Jelsch, V. R. Hathwar and T. N. Guru Row, *Cryst. Growth Des.*, 2010, **10**, 1516–1526.
- E. Espinosa, E. Molins and C. Lecomte, *Chem. Phys. Lett.*, 1998, **285**, 170–173.
- D. Cremer and E. Kraka, *Angew. Chem., Int. Ed.*, 1984, **23**, 627–628.
- A. A. El-Emam and J. Lehmann, *Monatsh. Chem.*, 1994, **125**, 587–591.
- R. C. Clark and J. S. Reid, *Acta Crystallogr., Sect. A: Found. Crystallogr.*, 1995, **51**, 887–897.
- O. V. Dolomanov, L. J. Bourhis, R. J. Gildea, J. A. K. Howard and H. Puschmann, *J. Appl. Crystallogr.*, 2009, **42**, 339–341.
- G. Sheldrick, *Acta Crystallogr., Sect. A: Found. Adv.*, 2015, **71**, 3–8.
- G. Sheldrick, *Acta Crystallogr., Sect. C: Struct. Chem.*, 2015, **71**, 3–8.
- M. J. Turner, J. J. McKinnon, S. K. Wolff, D. J. Grimwood, P. R. Spackman, D. Jayatilaka and M. A. Spackman, *CrystalExplorer17*, University of Western Australia, 2017.
- M. J. Frisch, G. W. Trucks, H. B. Schlegel, G. E. Scuseria, M. A. Robb, J. R. Cheeseman, G. Scalmani, V. Barone, B. Mennucci, G. A. Petersson, H. Nakatsuji, M. Caricato, X. Li, H. P. Hratchian, A. F. Izmaylov, J. Bloino, G. Zheng, J. L. Sonnenberg, M. Hada, M. Ehara, K. Toyota, R. Fukuda, J. Hasegawa, M. Ishida, T. Nakajima, Y. Honda, O. Kitao, H. Nakai, T. Vreven, J. A. Montgomery Jr, J. E. Peralta, F. Ogliaro, M. J. Bearpark, J. Heyd, E. N. Brothers, K. N. Kudin, V. N. Staroverov, R. Kobayashi, J. Normand, K. Raghavachari, A. P. Rendell, J. C. Burant, S. S. Iyengar, J. Tomasi, M. Cossi, N. Rega, N. J. Millam,



- M. Klene, J. E. Knox, J. B. Cross, V. Bakken, C. Adamo, J. Jaramillo, R. Gomperts, R. E. Stratmann, O. Yazyev, A. J. Austin, R. Cammi, C. Pomelli, J. W. Ochterski, R. L. Martin, K. Morokuma, V. G. Zakrzewski, G. A. Voth, P. Salvador, J. J. Dannenberg, S. Dapprich, A. D. Daniels, Ö. Farkas, J. B. Foresman, J. V. Ortiz, J. Cioslowski and D. J. Fox, *Gaussian 09, Revision D.01*, Gaussian, Inc., Wallingford, CT, 2013.
- 27 A. K. Todd, *AIMALL version 19.02.13*, TK Gristmill Software, Overland Park KS, USA, 2019.
- 28 Y. Zhao and D. G. Truhlar, *Theor. Chem. Acc.*, 2008, **120**, 215–241.
- 29 S. Grimme, J. Antony, S. Ehrlich and H. Krieg, *J. Chem. Phys.*, 2010, **132**, 154104.
- 30 A. D. Bochevarov, E. Harder, T. F. Hughes, J. R. Greenwood, D. A. Braden, D. M. Philipp, D. Rinaldo, M. D. Halls, J. Zhang and R. A. Friesner, *Int. J. Quantum Chem.*, 2013, **113**, 2110–2142.
- 31 (a) A. D. Becke, *J. Chem. Phys.*, 1993, **98**, 5648–5652; (b) C. Lee, W. Yang and R. G. Parr, *Phys. Rev. B: Condens. Matter Mater. Phys.*, 1988, **37**, 785–789; (c) S. H. Vosko, L. Wilk and M. Nusair, *Can. J. Phys.*, 1980, **58**, 1200–1211; (d) P. J. Stephens, F. J. Devlin, C. F. Chabalowski and M. J. Frisch, *J. Phys. Chem.*, 1994, **98**, 11623–11627.
- 32 F. A. Bulat, A. Toro-Labbé, T. Brinck, J. S. Murray and P. Politzer, *J. Mol. Model.*, 2010, **16**, 1679–1691.
- 33 D. Cremer and J. A. Pople, *J. Am. Chem. Soc.*, 1975, **97**, 1354–1358.
- 34 A.-M. S. Al-Tamimi, A. M. Alafeefy, A. A. El-Emam, S. W. Ng and E. R. T. Tiekink, *Acta Crystallogr., Sect. E: Struct. Rep. Online*, 2013, **69**, o683.
- 35 (a) C. F. Matta, J. Hernández-Trujillo, T. H. Tang and R. F. W. Bader, *Chem.-Eur. J.*, 2003, **9**, 1940–1951; (b) C. F. Matta, in *Hydrogen Bonding-New Insights*, ed. S. Grabowski, Springer, 2006, ch. 9, pp. 337–375; (c) I. Cukrowski and C. Matta, *Chem. Phys. Lett.*, 2010, **499**, 66–69.
- 36 J. Bernstein, R. E. Davis, L. Shimon and N.-L. Chang, *Angew. Chem., Int. Ed.*, 1995, **34**, 1555–1573.
- 37 L. H. Al-Wahaibi, N. S. Kumar, A. A. El-Emam, N. S. Venkataramanan, H. A. Ghabbour, A.-M. S. Al-Tamimi, J. Percino and S. Thamocharan, *J. Mol. Struct.*, 2018, **1175**, 230–240.
- 38 CSD search criteria: (i) 3D coordinates determined (ii) R-factor ≤ 0.05 (iii) not disordered (iv) no errors (v) not polymeric (vi) no ions (vii) no powder structures and (viii) only organic compounds.
- 39 L. Fábán and A. Kálmán, *Acta Crystallogr., Sect. B: Struct. Sci.*, 1999, **55**, 1099–1108.
- 40 (a) T. Gelbrich and M. B. Hursthouse, *CrystEngComm*, 2005, **7**, 324–336; (b) T. Gelbrich and M. B. Hursthouse, *CrystEngComm*, 2006, **8**, 448–460; (c) T. Gelbrich, T. L. Threlfall and M. B. Hursthouse, *CrystEngComm*, 2012, **14**, 5454–5464.
- 41 P. Politzer and J. S. Murray, *Cryst. Growth Des.*, 2015, **15**, 3767–3774.
- 42 (a) P. Politzer, J. S. Murray and T. Clark, *Phys. Chem. Chem. Phys.*, 2013, **15**, 11178–11189; (b) T. Clark, M. Hennemann, J. S. Murray and P. Politzer, *J. Mol. Model.*, 2007, **13**, 291–296.
- 43 P. L. A. Popelier, *J. Phys. Chem. A*, 1998, **102**, 1873–1878.
- 44 E. Espinosa, I. Alkorta, J. Elguero and E. Molins, *J. Chem. Phys.*, 2002, **117**, 5529–5542.

